Modeling techniques to study CO$_2$-injection induced micro-seismicity

Induced micro-seismicity

José M. Carcione[1] · **Federico Da Col**[1] ·
Gilda Currenti[2] · **Barbara Cantucci**[3]

Abstract CO$_2$ injection in saline aquifers is one solution to avoid the emission of this greenhouse gas to the atmosphere. This process induces a pore-pressure build-up around the borehole that generates tensile and shear micro-earthquakes which emit P and S waves if given pressure thresholds are exceeded. Here, we develop a simple model to simulate micro-seismicity in a layer saturated with brine, based on an analytical solution of pressure diffusion and an emission criterion for P and S waves. The model is based on poroelasticity and allows us to obtain estimations of the hydraulic diffusivity on the basis of the location of the micro-earthquakes (defining the CO$_2$ plume) and the triggering time. Wave propagation of P and S waves is simulated with a full-wave solver, where each emission point is a source proportional to the difference of the pore pressure and the tensile and shear pressure thresholds. Finally a reverse-time migration algorithm is outlined to locate the asynchronous sources induced by the fluid flow, determinated by the maximum amplitude at each cell versus the back propagation time.

1 Introduction

Geological storage is an immediate option to solve in part the problem of CO$_2$ emission to the atmosphere. Practical choices are injection into hydrocarbon reservoirs and saline aquifers (e.g., Arts et al., 2004; Carcione et al., 2006). It is essential to monitor the injected plumes as they diffuse into the reservoir, and any leakage has to be carefully detected. Active seismic methods can be used for a non-invasive location of the CO$_2$ plume (e.g., Carcione et al., 2012). On the other hand, passive seismic emission caused

[1]Istituto Nazionale di Oceanografia e di Geofisica Sperimentale (OGS), Borgo Grotta Gigante 42c, 34010 Sgonico, Trieste, Italy. E-mail: jcarcione@inogs.it
[2] Istituto Nazionale di Geofisica e Vulcanologia (INGV) – Sezione di Catania, Catania, Italy.
[3] Istituto Nazionale di Geofisica e Vulcanologia (INGV) – Sezione di Roma, Sismologia e Tettonofisica, Roma, Italy.

by fluid injection can also be used, on the basis of the induced micro-cracks by the fluid front (e.g., Vesnaver et al., 2010; Oye et al., 2013), since the fluid pressure may exceed the fracture pressure in many parts of the reservoir and emit P and S waves. In fact, induced seismic events of low magnitude are present during and after the injection (e.g., Urbancic et al., 2009; Oye et al., 2013; Martinez-Garzón et al., 2013). Moreover, micro-seismic data can be used to estimate the hydraulic diffusivity of the medium (Shapiro et al., 1997; Angus and Verdon, 2013).

In this study, we first obtain the tensile and shear seismic sources generated by CO_2 injection in an infinite layer on the basis of an analytical solution of pressure diffusion obtained by Mathias at al. (2011) and an emission criterion based on the stiffness properties of the medium. Fluid injection in a borehole causes an increase of the pore pressure in rocks, which implies a decrease of the effective stress, which, low enough, can trigger micro-earthquakes in zones of weakness. Tensile and shear failure occur as a consequence of the injection (Rutqvist et al., 2008; Stanchits et al., 2011) and the common criterion to decide failure is based on a critical fluid pressure for fracturing that exceeds a given tectonic stress. Rutqvist et al. (2008) conclude that it is essential to have an accurate estimate of the in situ stress field to use this criterion. It is easier to establish the failure criterion on the basis of the strength of the rock, since this information (stiffness moduli) can be obtained from seismic data. The criterion we adopt here is the following. If the pore pressure exceeds the tensile and/or shear strength of the rock, defined by very small Young and shear moduli, there is emission whose strength is proportional to the excess pressure. These thresholds are assumed to vary on a fractal manner based on the von-Kármán correlation function (e.g., Carcione and Gei, 2009). **Langenbruch and Shapiro (2014) show that the elastic heterogeneity of rocks obtained from sonic and density logs along boreholes cause significant fluctuations of fracture reactivation and opening pressures. As a result fluctuations of principal stress magnitudes are of fractal nature. Correlation lengths of 1 m are assumed on the basis that the heterogeneities are smaller than the wavelength of a seismic signal. In the case of fine layering values from tens of cm to 1 m are realistic.** The stiffness moduli can be obtained from seismic and sonic-log data or from ultrasonic experiments on cores. Other criteria exist to determine the emission, for instance, Rozhko (2010) uses the effective-stress law and the Coulomb yielding stress; the parameters are obtained from geo-mechanical triaxial laboratory measurements. **Application of the injection technology near urban areas may involve seismic hazards (e.g., Sminchak et al., 2001). Supercritical CO_2 is lighter than water and may cause pressure buildup leading to seismicity. The injection pressure at the wellhead should not exceed a maximum which has to be calculated to assure that the pore pressure does not initiate new fractures or propagate existing fractures inducing micro-earthquakes of a given magnitude.**

The hydraulic diffusivity of the medium can be obtained from the envelope of events by representing the distance of the events to the injection point as a function of the emission times. The calculated diffusivity can then be used to estimate the formation permeability. Then, we simulate wave propagation of P and S waves, by using a forward modeling algorithm based on the pseudospectral method (Carcione et al., 2006; Carcione, 2015), to obtain microseismic data. Finally, we consider the location of the microseismic sources. A partial review of the method used so far to locate hypocenters of microseismic data can be found in Haldorsen et al. (2013). In particular they use a full-waveform migration algorithm and an imaging condition based on "a semblance-

weighted deconvolution between two or more reconstructed source signatures, requiring similarity and simultaneity of the reconstructed signatures". It is not clear if this method deals with asynchronous sources. Here, we outline an automatic technique to image asynchronous micro-earthquake sources, which should provide an image of the CO_2 cloud, by using reverse-time migration based on the Fourier pseudospectral method (e.g., Baysal et al., 1983).

2 The model

The model is based on an analytical solution to obtain the pore pressure around the injection point (Mathias et al., 2011) and an criterion for the emission of P and S waves. We simulate the distribution of injection-induced micro-seismicity that depends on the stiffness properties of the medium and the spatial distributions of emission sources follows a fractal law (Rothert and Shapiro, 2003).

2.1 Pressure buildup

To obtain the pore pressure around a well due to CO_2 injection in a brine saturated formation, we use the analytical solution (Sol. 1, immiscible fluids) derived by Mathias et al. (2009a,b). This solution gives the pressure as a function of time and radial (horizontal) distance in a formation of thickness H and radius R. The solution, subject to an initial pressure p_i and constant injection rate m_0, is given in Appendix A.

2.2 Emission criterion

Induced seismicity by fluid injection in a porous rock depends on the properties of the medium, basically on the relation between the fluid pressure and the elastic properties of the skeleton. When the fluid pressure reaches the fracture pressure, the dry-rock stiffnesses decrease dramatically (e.g., Shapiro, 2003; Carcione et al., 2006). A realistic expression of the dry-rock Young and shear moduli, Y_m and μ_m, respectively, has the form

$$A = a - b \exp(-p_e/p^*), \quad p_e = p_c - np \tag{1}$$

(Shapiro, 2003; Carcione, 2015), where p_c, p and p_e are the confining, pore and effective pressures, respectively, a, b and p^* are constants, and n is the effective stress coefficient. Constants a, b, p^* and n define the strength of the medium to an applied pore pressure and are found by fitting experimental data versus confining and pore pressures.

The rock emits elastic energy at a given fracture pressure P, which we assume to occur at a small stiffness, i.e., if $A = \gamma a$, where $\gamma \ll 1$. Then,

$$P = \frac{1}{n} \left(p_c - p^* \ln \frac{b}{a(1-\gamma)} \right). \tag{2}$$

$Y_m = \mu_m = \gamma a$ imply tensile and shear sources, respectively, whose strength is proportional to the pressure difference $p - P_T$ (tensile) and $p - P_S$ (shear). There is tensile emission when $p > P_T$ and shear emission when $p > P_S$. **The confining pressure**

is related to the vertical stress. It is implicitly assumed that there is a differential stress and/or anisotropy (vertical compaction) to generate shear failure.

Rutqvist et al. (2008) found that shear failure usually occurs at a lower injection pressure than tensile hydro-fracturing. We assume that $P_S < P_T$ and a fractal behaviour of these thresholds around an average value obtained from equation (2). Then, we apply the procedure described in Appendix B. **The approach is different from that of Rothert and Shapiro (2003), who consider only reactivation of pre-existing fractures and no tensile opening. These authors discretize the space and consider a single threshold. Here, each cell emits only one time; after the cell has emitted its stiffness is set to a very high value.**

Rocks are in a subcritical state of stress in some regions. Fracture occurs when the pore pressure is close but smaller than the confining pressure. At the fracture pressure the rock starts to break which means that the rock stiffness is approximately zero but not zero. Once determined the fracture pressure, the threshold stiffness can be determined from equation (1). Most fracture models are based on equations of the form $P = k(p_c - p) + p$ (Hubbert and Willis (1957), where k is the effective stress ratio (also termed matrix stress coefficient) set to $k=1/3$ by Hubbert and Willis (1957) but allowed to vary with depth, in the range 0.3-1.0, by Pennebaker (1968), from values of 0.3 for shallow layers to values near 1.0 at depths. Moreover, fracture pressures can vary randomly according to the rock stiffness locally. Here, we consider variations as in Rother and Shapiro (2003).

2.3 Seismic modeling

The synthetic seismograms are computed with a modeling code based on an isotropic and viscoelastic stress-strain relation. The equations are given in Section 3.9 of Carcione (2015) and the algorithm is based on the Fourier pseudospectral method for computing the spatial derivatives and a 4th-order Runge-Kutta technique for calculating the wavefield recursively in time. The differential equations are outlined in Appendix C. Each micro-earthquake is triggered at the emission time and location dictated by the injection pressure, generating P and S waves which are recorded at the surface.

3 Example

We consider the Utsira Sand formation at the Sleipner field in the North Sea. At the injection site it has 280 m thickness (top at 820 m and bottom 1100 m b.s.l.). The sea bottom is located at nearly $z_b = 100$ m depth and the caprock is a sealing unit, a silty-mudstone layer 200 m thick approximately (Arts et al., 2008). We consider an injection point in the middle of the aquifer at $z_0 = 960$ m. The hydrostatic pressure is $p_H = \rho_w g z$, with $\rho_w = 1040$ kg/m^3 the density of brine and $g = 9.81$ m/s^2, the gravity constant. We obtain 8.4 MPa, 9.8 MPa and 11.2 MPa at the top, z_0 and bottom, respectively. The confining pressure is $p_c = \rho_w g z_b + \bar{\rho} g(z - z_b)$, where $\bar{\rho} = 2100$ kg/m^3 is the average sediment density (taken from well logs). We obtain 15.8 MPa, 18.8 MPa and 21.6 MPa at the top, z_0 and bottom, respectively.

The properties to simulate the injection are given in Table 1. The permeability is an effective value because the formation contains low-permeability mudstone layers (Arts et al., 2008). The analytical solution (Mathias et al., 2011) is compared to numerical simulations using the TOUGH2 ECO2N commercial software (Pruess et al., 1999; Pruess, 2005), which also considers thermal effect by solving in addition the heat transport equation. The model assumes the following relationship between brine effective saturation S_e and capillary pressure p_{cp}:

$$S_e = \left(1 + \left|\frac{p_{cp}}{p_{c0}}\right|^{1/(1-m)}\right)^{-m}, \quad \text{with} \quad S_e = \frac{1 - S - S_r}{1 - S_r} \tag{3}$$

(van Genuchten, 1980), where p_{c0} and m are the van Genuchten parameters. Linear relative permeability functions are assumed for the gas and brine phases:

$$\kappa_{rw} = \kappa_{rw0}\left(\frac{1 - S - S_r}{1 - S_{gc} - S_r}\right), \quad \kappa_r = \kappa_{rg0}\left(\frac{S - S_{gc}}{1 - S_{gc} - S_r}\right), \tag{4}$$

where S_{gc} is the critical gas saturation and κ_{rw0} and κ_{rg0} are the end-point relative permeabilities. The properties used by the TOUGH2 code are: $p_{c0} = 19.6$ kPa, $m = 0.46$, $S_{gc} = 0$, $\kappa_{rw0} = 1$, $\kappa_{rg0} = 0.3$, the grain density $\rho_s = 2650$ kg/m^3, the specific heat capacity $c_p = 1000$ J/kg/$^{\circ}$C and the thermal conductivity $k_r = 2.5$ W/m/$^{\circ}$C. The system is assumed to be initially free of CO_2 at a temperature of 40 $^{\circ}$C with an hydrostatic pressure uniformly distributed in the radial direction. The reservoir obeys at its sides impermeable and adiabatic boundary conditions. The constant mass flux m_0 of pure supercritical CO_2 is injected at the well boundary. The radially symmetric computational domain is vertically divided in 14 equally spaced layers of 20 m thickness. In the radial direction, the domain is divided in 456 cells, whose spacing is finer (5 mm) near the well and coarser (1500 m) at the outermost boundary. **The radial symmetry makes the problem basically two-dimensional**. Figure 1 shows the pressure (a) and saturation (b) profiles for different injection times. Comparisons with these non-isothermal numerical results confirm that the analytical iso-thermal solution provides acceptable estimates of pressure buildup.

We assume that at infinite effective pressure the dry-rock moduli are given by the upper limits

$$K_0 = K_s(1 - \phi) \quad \text{and} \quad \mu_0 = \mu_s(1 - \phi) \tag{5}$$

where $K_s = 37$ GPa and $\mu_s = 35$ GPa are the grain bulk and shear moduli, (Carcione et al., 2006). Since the Young modulus is related to the bulk and shear moduli as $Y = 9K\mu/(3K + \mu)$, we obtain $K_0 = 23.7$ GPa, $\mu_0 = 22.4$ GPa and $Y_0 = 51.1$ GPa. The moduli (1),

$$Y_m = 51.1 - 50.6\exp(-p_e/0.35) \quad \text{and} \quad \mu_m = 22.4 - 22.37\exp(-p_e/0.30), \tag{6}$$

with $n = 0.8$ yields $K_m = 1.37$ GPa and $\mu_m = 0.82$ GPa at $z = z_0$, are in agreement with the experimental values (Carcione et al., 2006), where a and b are given in GPa and p^* is given in MPa in equation (6). Assuming $\gamma = 0.03$, the mean values (2) are

$$P_T = 14.4 \text{ MPa} \quad \text{and} \quad P_S = 12.4 \text{ MPa}. \tag{7}$$

Figure 2 shows a vertical section of the fractal distribution of P_T, where the medium has 375×375 cells with a grid spacing of 100 m/375 = 0.26 m along the horizontal and

vertical directions. The fractal parameters are $P_0 = P_T$ ($P_0 = P_S$ in the shear case), with $\Delta P_m = 60\ \%\ P_0$, $\nu = 0.18$, $l = 1$ m and $d = 2$. If P_T or P_S are smaller or equal than 9.94 MPa (slightly above p_i), we set their value to 9.94 MPa, since at hydrostatic values of the pore pressure we assume no emission. Figure 3 shows the tensile (a) and shear (a) emission sources after one hour of injection, where the events are 4006 and 22009, respectively.

The location of the events as a function of the emission time is represented in Figure 4, where the solid lines corresponds to

$$r = \sqrt{4\pi Dt} \qquad (8)$$

(Shapiro et al., 1997), with $D = 0.137$ m^2/s, where D is the hydraulic diffusivity. **It can be seen that from a distance of 50 m the density of events is strongly decreasing. This signature occurs due to the small spatial extent of the model. Moreover, there are many events at the distance of the triggering front. These events correspond to cells where the initially selected critical pressure is below the value of 9.94 MPa. The triggering front correspond to this isobar in both the shear and the tensile events. This is why the triggering front in both cases is identical. Thus, the difference of critical pressure magnitudes for tensile and shear events have only an effect on the density of the events.**

There is an equation based on poroelasticity to estimate the value of D. According to Biot theory, an approximation for a single fluid is

$$D = \frac{M E_m \kappa}{E_G \eta} \qquad (9)$$

(Shapiro et al., 1997; Carcione, 2015) where

$$
\begin{aligned}
M &= \frac{K_s}{1 - \phi - K_m/K_s + \phi K_s/K_f}, \\
E_m &= K_m + \frac{4}{3}\mu_m, \\
E_G &= E_m + \bar{\alpha}^2 M, \\
\bar{\alpha} &= 1 - \frac{K_m}{K_s},
\end{aligned}
\qquad (10)
$$

where K_f is an effective fluid bulk modulus. Assuming, $\phi = 0.36$, $K_m = 1.37$ GPa, $\mu_m = 0.82$ GPa, $K_s = 37$ GPa, $K_f = 0.3$ GPa and $\eta = 0.000963$ Pa s, we obtain D = 0.13 m^2/s, since the presence of CO_2 implies a lower value of K_f. Conversely, equation (9) can be used to estimate the permeability if the poroelastic properties and effective fluid modulus are known.

The numerical modeling theory to compute passive microseismograms is illustrated in Appendix C and the source implementation in Appendix D. We consider a numerical mesh with $n_x = n_z = 231$ grid points and a grid spacing $dx = dz = 5$ m. The medium is homogeneous with the properties $v_P = 1170$ m/s, $v_S = 650$ m/s and $\rho = 2017$ kg/m^3 (from equation (41), see below), matching those of the Utsira formation (Carcione et al., 2006). The source time history is

$$g(t) = \left(u - \frac{1}{2} \right) \exp(-u), \quad u = \left[\frac{\pi(t - t_s)}{T} \right]^2, \qquad (11)$$

where T is the period of the wave and we take $t_s = 1.4T$. The peak frequency is $f_p = 1/T = 25$ Hz. The time step of the Runge-Kutta algorithm is 1 ms. Tensile sources are described by equation (37) with $\delta = 0$ and shear sources are described by equation (38) with $\delta = \pi/2$. Daugherty and Urbancic (2009) report magnitudes M_w from -2.3 to 0 from events caused by CO_2 injection. Moment magnitude is related to the seismic moment M_0 as $M_0 = 10^{1.5M_w+9}$ for M_0 expressed in J (Joule). We consider events with $M_w = -1$, i.e., $M_0 = 10^{7.5}$ J, **although different magnitudes can be modeled as well.** Then, the non-zero components are $M_{zz} = 1.8$ MJ (tensile source) and $M_{xz} = 0.9$ MJ (shear source). Figure 5a shows a snapshot where the radiation pattern and relative amplitudes of the two types of sources can be observed. Theoretical expressions and representations of the radiation patterns are given in Vavryčuk (2011).

To illustrate a simulation, we consider the interval 3000 s to 3020 s, with 52 shear sources and 6 tensile sources. Figure 6 shows the model and a snapshot at 3000.5 s corresponding to the first three shear sources and a tensile source, all synchronous with onset times of 3000.056 s. The time parameter of the relaxation mechanisms is $\tau_0 = 1/(2\pi 25$ Hz$)$. In this simulation, absorbing strips are active to damp the wave fields reaching the sides, top and bottom of the mesh to avoid wraparound (50 nodes at the sides and 40 nodes in the vertical direction). The P-wave velocities are computed with the model outlined in Appendix E. For simplicity, we assume a formation with average dry-rock properties given by equations (39) and (40), with the properties reported above and $K_c = 25$ MPa (Carcione et al., 2006), $K_w = 2.63$ GPa, $\rho_s = 2650$ kg/m^3, $\rho_c = 869$ kg/m^3 and $\rho_w = 1040$ kg/m^3. Figure 7 shows the P- and S-wave velocities and bulk density as a function of the radial distance, based on the saturation shown in Figure 1b. Note the remarkable change in the velocity of the compressional wave due to the replacement of water near the well by CO_2 with a very low bulk modulus. However, at 3000 s the CO_2 is practically confined around a few meters from the well and the rest of the formation is still saturated with brine. The synthetic seismogram and time histories are shown in Figures 8a and 8b, respectively. The solid and dashed lines correspond to the receivers located at 330 m and 430 m and indicated with a letter V in the figure. The events correspond to the four sources whose snapshots are displayed in Figure 6. Figure 9 shows the time histories recorded at receivers 1 (left) and 2 (right) shown in Figure 8, where we have assumed lossless media, i.e., $Q_\nu = \infty$. The corresponding simulation in the lossy case is displayed in Figure 10, where it is clear that the wavefield has been attenuated and some events can be too weak to be detected. The P and S events of the 58 sources and the reverberations in the layer can be observed in these seismic traces.

Modeling is essential to map the location of the sources. Here, we briefly outline a possible method based on reverse-time migration and an imaging condition, that we shall develop in a future work in more detail. The algorithm is illustrated in Appendix F. To illustrate the method, we assume that the P and S wave fields have been separated. Let us consider a simple example consisting in three sources of dissimilar strength activated at different onset times. The mesh has 220×220 points with grid spacing of 10 m along the horizontal and vertical directions. The model (seismic velocity) is known. In this example, we consider a layer with a velocity of 2 km/s embedded in a background medium of velocity 2.5 km/s. The source central frequency is $f_p = 25$ Hz and $t_s = 1.2/f_p$. The forward modeling uses $dt = 1$ ms and the field is propagated 0.8 s and recorded at a horizontal line of receivers at 300 m depth. Figure 11 shows a snapshot at 320 ms (a) and the seismogram (b), where we can see that each source is activated at different times. Each source has a different strength: in relative terms it

is 1.2 (source 1), 1 (source 2) and 1.5 (source 3). In Figure 11a, from left to right the source-onset times have a delay of 0, 160 ms and 100 ms, while their maxima have a delay of 49, 209 and 149 ms, respectively, where 49 is t_s/dt (see equation (11)). Then, a proper imaging of each source occurs by back propagating (800 - 49) ms = 751 ms (source 1), (800 - 209) ms = 591 ms (source 2) and (800 - 149) ms = 651 ms (source 3), where 800 ms is the maximum propagation time of the seismogram.

We represent in Figure 12 the maximum amplitudes of the images as a function of the back propagation times, where the three maxima correspond to the sources. The maxima occur at the grid points where the sources were implemented. The reverse-time migration images are shown in Figure 13. The source numbers and propagation times for an optimal focusing are indicated. It is clear that when the wave field is focused almost at a point, a source has been located. The method is far from perfect since wave-field constructive interference can enhance the amplitudes at some points where no source is present. Therefore, this imaging method can miss some sources of the CO_2 cloud. A pattern recognition algorithm could be used in addition to determine the source locations (Joswig, 1990) or an alternative technique, as for instance, seismic interference (Sava, 2011).

Future work involves the use of more general simulations (e.g. Carcione et al., 2014) and commercial software, such as TOUGH2, to model fluid flow in heterogeneous media (e.g., Audigane et al., 2011).

4 Conclusions

Fluid-flow simulation and seismic methods are essential to monitor the presence of CO_2 after and during the injection in geological formations. The success of the methodology is subject to a correct description of the physical processes involved and use of integrated geophysical methods. We propose a simple analytical model to describe the pore-pressure build-up in a layer due to the injection and describe the emission of seismic events due to the generation of micro cracks based on a criterion that takes into account the stiffness moduli of the host rock. A poroelastic model allows us to obtain the hydraulic diffusivity and permeability of the formation on the basis of the location and onset time of the seismic events. We then introduce a realistic forward modeling algorithm to simulate P- and S-wave propagation, where each source strength and radiation pattern is determined by the pore pressure and a generalized moment-tensor theory, respectively. Finally, we propose an algorithm to map the location of the multiple sources, approximating the CO_2 cloud, based on a reverse-time migration algorithm and an imaging condition, where optimal focusing (maximum amplitude) of the wave field back propagated in time occurs.

References

1. Abramowitz, M., and Stegun, I. A., 1964, Handbook of mathematical functions, National Bureau of Standards, Applied Mathematical Series.

2. Angus, D. A., and Verdon, J. P., 2013, Using microseismicity to estimate formation permeability for geological storage of CO2, Geophysics, doi:10.1155/2013/160758.

3. Arts, R. J., Chadwick, A., Eiken, O., Thibeau, S., and Nooner, S., 2008, Ten years' experience of monitoring CO_2 injection in the Utsira Sand at Sleipner, offshore Norway, First Break, 26, 65-72.

4. Audigane, P., Chiaberge, C., Mathurin, F., Lions, J., Picot-Colbeaux, G., 2011, A workflow for handling heterogeneous 3D models with the TOUGH2 family of codes: Applications to numerical modeling of CO2 geological storage, Computers & Geosciences, 37, 610-620.

5. Baysal, E., Kosloff, D. D., and Sherwood, J. W. C., 1983, Reverse time migration, Geophysics, 48, 1514-1524.

6. Carcione, J. M., 2015, Wave Fields in Real Media. Theory and numerical simulation of wave propagation in anisotropic, anelastic, porous and electromagnetic media, 3rd edition, Elsevier.

7. Carcione, J. M., Böhm G., and Marchetti, A., 1994, Simulation of a CMP seismic section, Journal of Seismic Exploration, 3, 381-396.

8. Carcione, J. M., Cavallini, F., Gei, D. and Botelho, M. A. B., 2014, Moment-tensor point source implementation in direct grid methods, Journal of Earthquake Engineering, in print.

9. Carcione, J. M., Finetti, I., and Gei, D., 2003, Seismic modeling study of the Earth's deep crust, Geophysics, 68, 656-664.

10. Carcione, J. M., and Gei, D., 2009, Theory and numerical simulation of fluid-pressure diffusion in anisotropic porous media, Geophysics, 74, N31-N39.

11. Carcione, J. M., Gei, D., Picotti, S., and Michelini, A., 2012, Cross-hole electromagnetic and seismic modeling for CO2 detection and monitoring in a saline aquifer, Journal of Petroleum Science and Engineering., 100, 162-172.

12. Carcione, J. M., Helle, H. B., Seriani, G., and Plasencia, M. P., 2005, On the simulation of seismograms in a viscoelastic Earth by pseudospectral methods, Geophys. Internat., 44, 123-142.

13. Carcione, J. M., Picotti, S., Gei, D., and Rossi, G., 2006, Physics and seismic modeling for monitoring CO_2 storage, Pure and Applied Geophysics, 163, 175-207.

14. Carcione, J. M., Picotti, S., Santos, J. E., Qadrouh, A. N., and Almalki, H. S., 2014, Numerical simulation of two-phase fluid flow, J. Petrol. Explor. Prod. Technol., DOI 10.1007/s13202-014-0109-y.

15. Daugherty, J., and Urbancic, T., 2009, Passive microseismics: A valuable technique for monitoring CO_2 injections, AAPG Hedberg Conference "Geological Carbon Sequestration: Prediction and Verification", Vancouver, BC, Canada

16. Gajewski, D., and Tessmer, E., 2005, Reverse modelling for seismic event characterization, Geophys J. Int., 163, 276-284.

17. **Gangi, A. F., and Carlson, R. L., 1996, An asperity-deformation model for effective pressure, Tectonophysics, 256, 241-251.**

18. Haldorsen, J. B. U., Brooks, N. J., and Milenkovic, M., 2013, Locating microseismic sources using migration-based deconvolution Geophysics, 78, KS73-KS84.

19. **Holliger, K., 1997, Seismic scattering in the upper crystalline crust based on evidence from sonic logs, Geophys. J. Internat., 128, 65-72.**

20. **Hubbert, M. K. and Willis, D. G., 1957, Mechanics of hydraulic fracturing, AIME Petroleum Transactions, 210, 153-168.**

21. **Hummel, N., and Shapiro, S., 2012, Microseismic estimates of hydraulic diffusivity in case of non-linear fluid-rock interaction, Geophysical Journal International, 188, 1441-1453.**

22. Joswig, M., 1990, Pattern recognition for earthquake detection, Bull. Seism. Soc. Am. 80, 170-186.

23. **Langenbruch, C., and S.A. Shapiro, S. A., 2014, Gutenberg-Richter relation originates from Coulomb stress fluctuations caused by elastic rock heterogeneity, Journal of Geophysical Research Solid Earth, 119(2), 1220-1234.**

24. Martínez-Garzón, P., Bohnhoff, M., Kwiatek, G., Zambrano-Narváez, G., and Chalaturnyk, R., 2013, Microseismic monitoring of CO_2 injection at the Penn West Enhanced Oil Recovery Pilot Project, Canada: Implications for detection of wellbore leakage, Sensors, 13, 11522-11538.
25. Mathias, S. A., Hardisty, P. E., Trudell, M. R., and Zimmerman, R. W., 2009a, Approximate solutions for pressure buildup during CO2 injection in brine aquifers, Transp. Porous Media, 79, 265-284
26. Mathias, S. A., Hardisty, P. E., Trudell, M. R., and Zimmerman, R. W., 2009b, Screening and selection of sites for CO2 sequestration based on pressure buildup, Int. J. Greenhouse Gas Control, 3(5), 577-585. Erratum: 4 (2010) 108-109.
27. Mathias, S. A., González Martínez de Miguel, G. J., Thatcher, K. E. and Zimmerman, R. W., 2011, Pressure buildup during CO2 injection into a closed brine aquifer, Transp Porous Media, 89, 383-397.
28. McMechan, G.A., 1982, Determination of source parameters by wavefield extrapolation, Geophys. J. R. astr. Soc., 71, 613-628.
29. Oye, V., Aker, E., Daley, T. M., Kühn, D., Bohloli, B., and Korneev, V., 2013, Microseismic monitoring and interpretation of injection data from the In Salah CO2 storage site (Krechba), Algeria, Energy Procedia, 37, 4191-4198.
30. **Palmer, I. D, and Mansoori, J., 1998, How permeability depends upon stress and pore pressure in coalbeds: A new model, SPE Reservoir Evaluation & Engineering, December Issue, 539-543.**
31. **Pennebaker, E.S., 1968, An engineering interpretation of seismic data, SPE # 2165.**
32. Pruess, K., Oldenburg, C. M., Moridis, G., 1999, TOUGH2 users guide, version 2.0. Report LBNL-43134, Lawrence Berkeley National Laboratory, Berkeley, CA, USA.
33. Pruess, K.:, 2005, ECO2N: A TOUGH2 fluid property module for mixtures of water, NaCl, and CO2. Report LBNL-57952, Lawrence Berkeley National Laboratory, Berkeley, CA, USA (2005)
34. Robertsson, J. O. A. and Curtis, A., 2002, Wavefield separation using densely deployed threecomponent singlesensor groups in land surfaceseismic recordings, Geophysics,. 67, 1624-1633.
35. Rothert, E. and Shapiro, S.A., 2003, Microseismic monitoring of borehole fluid injections: data modelling and inversion for hydraulic properties of rocks, Geophysics, 68(2), 685-689.
36. Rozhko, A. Y., 2010, Role of seepage forces on seismicity triggering, J. Geophys. Res. B, vol. 115, no. 11, Article ID B11314, 2010.
37. Rutqvist, J., Birkholzer, J. T. and Tsang, C.-F., 2008, Coupled reservoir–geomechanical analysis of the potential for tensile and shear failure associated with CO2 injection in multilayered reservoir–caprock systems, Rock Mechanics and Mining Sciences 45, 132-143.
38. Sava, P., 2011, Micro-earthquake monitoring with sparsely sampled data, J. Petrol. Explor. Prod. Technol., 1, 43-49.
39. Shapiro, S. A., 2003, Elastic piezosensitivity of porous and fractured rocks, Geophysics, 68, 482-486.
   Shapiro, S. A., and Dinske, C., 2009, Scaling of seismicity induced by nonlinear fluid-rock interaction, Journal of Geophysical Research Solid Earth, 114, B09307, doi:10.1029/2008JB006145.
40. Shapiro, S. A., Huenges, E. and Borm, G., 1997, Estimating the permeability from fluid-injection induced seismic emission at the KTB site, Geophys J. Internat, 131, F15-F18, see also Corrigendum, Geophys J. Internat., 134, 913.
   Sminchak, J., Gupta, N., and Byrer, C., 2001, Issues Related to Seismic activity Induced by the Injection of CO2; in Deep Saline Aquifers, NETL Proceedings of First National Conference on Carbon Sequestration.
41. Stanchits, S., Mayr, S., Shapiro, S., and Dresen, G., 2011, Fracturing of porous rock induced by fluid injection, Tectonophysics, 503, 129-145
42. Urbancic, T. I., Daugherty, Bowman, J. S., and Prince, M., 2009, Microseismic monitoring of a carbon sequestration field test, in Proceedings of the 2nd EAGE Passive Seismic Workshop, Limassol, Cyprus.
43. van Genuchten, M. T., 1980, A closed form equation for predicting the hydraulic conductivity of unsaturated soils, Soil. Sci. Soc. Am. J., 44, 892-898.
44. Vavryčuk, V., 2011, Tensile earthquakes: Theory, modeling, and inversion, J. Geophys. Res., B12320, doi:10.1029/2011JB008770.

45. Vesnaver, A., Lovisa, L. and Böhm, G., 2010, Joint 3D processing of active and passive seismic data, Geophys. Prosp., 58, 831-844.

46. Zhu, T., Harris, J. M., and Biondi, B., 2014, Q-compensated reverse-time migration, Geophysics, 79, S77-S87.

Table 1. Material properties and dimensions.

ϕ	0.36
κ	0.2 D
κ_r	0.3
C_w	0.38 1/GPa
$C_r = 1/K_m$	0.73 1/GPa
η	0.0847×10^{-3} Pa s
η_w	0.000963 Pa s
ρ_c	869 kg/m^3
S_r	0.5
m_0	300 Kg/s
p_i	9.8 MPa
r_0	0.2 m
H	280 m
R	20 km
b	0
b_r	0

A Solution of the pressure equation

We use the solution obtained by Mathias et al. (2009a,b, 2011) to model the pressure buildup in a layer of thickness H and finite radial extent around a well, subject to a constant injection rate. The assumptions are i) The pressure is constant along the vertical direction, ii) Capillary pressure are neglected, ii) The CO$_2$ and brine phases are immiscible, iv) Relative permeability is linear with the saturation, iv) The properties are uniform, and v) The radial extent is much greater than the hole radius. On the basis of the list of symbols give below, the solution is

$$\hat{p}(t,r) = \mathrm{E}(2/\gamma) - \frac{1}{2}\ln\left(\frac{x}{2\gamma}\right) - 1 + \frac{1}{\gamma} + \frac{\beta}{\sqrt{x\hat{t}}}, \quad x \leq 2\gamma$$

$$= \mathrm{E}(2/\gamma) - \sqrt{\frac{x}{2\gamma}} + \frac{1}{\gamma}, \qquad\qquad 2\gamma < x < 2/\gamma, \tag{12}$$

$$= \mathrm{E}(x), \qquad\qquad x \geq 2/\gamma$$

where

$$\mathrm{E}(x) = \frac{1}{2\gamma} E_1\left(\frac{\alpha x}{4\gamma}\right) \qquad\qquad \hat{t} \leq \hat{t}_c,$$

$$= \frac{2\hat{t}}{\alpha\hat{R}^2} - \frac{1}{\gamma}\left[\frac{3}{4} - \frac{1}{2}\ln\left(\frac{\hat{R}^2}{x\hat{t}}\right) - \frac{(\gamma x - 2)\hat{t}}{2\gamma\hat{R}^2}\right], \quad \hat{t} > \hat{t}_c, \tag{13}$$

where $E_1(x) = -\mathrm{Ei}(-x)$ is the exponential integral, and

$$\hat{t} = \frac{m_0 t}{2\pi(1 - S_r)\phi H r_0^2 \rho_c}, \quad \gamma = \frac{\eta}{\kappa_r \eta_w}, \qquad \hat{R} = \frac{R}{r_0},$$

$$\hat{p} = \frac{2\pi H \rho_c \kappa_r \kappa(p - p_i)}{m_0 \eta}, \quad \hat{r} = \frac{r}{r_0}, \qquad \hat{t}_c = \frac{\alpha\hat{R}^2}{2.246\gamma}, \tag{14}$$

$$\alpha = \frac{m_0 \eta(C_r + C_w)}{2\pi(1 - S_r)H\rho_c\kappa_r\kappa}, \quad \beta = \frac{m_0\kappa_r\kappa b_r b}{2\pi H r_0 \eta}, \quad x = \frac{\hat{r}^2}{\hat{t}}.$$

Equation (13) assumes that the radial extent of the CO_2 plume is much smaller than R (closed formation). The whole solution corresponds to Eqs. 20 and 42 in Mathias et al. (2011).

Mathias et al. (2009a)(Eq. 26) provide a solution for the CO_2 brine interface elevation, which translated to CO_2 saturation is

$$
\begin{aligned}
S &= 1 - S_r, & x \leq 2\gamma \\
&= \frac{1 - S_r}{\gamma - 1} \left(\gamma - \sqrt{\frac{2\gamma}{x}} \right), & 2\gamma < x < 2/\gamma, \\
&= 0, & x \geq 2/\gamma.
\end{aligned}
\tag{15}
$$

This solution is valid for $\alpha \ll 1$.

The symbols are defined as follows.

$$
\begin{aligned}
b &= \text{Forchheimer parameter, m}^{-1} \\
b_r &= \text{Relative Forchheimer parameter} \\
C_r &= \text{Rock compressibility, (Pa)}^{-1} \\
C_w &= \text{Brine compressibility, (Pa)}^{-1} \\
\eta &= CO_2 \text{ viscosity, Pa s} \\
\eta_w &= \text{Brine viscosity, Pa s} \\
\kappa_r &= CO_2 \text{ relative permeability} \\
\kappa &= \text{Permeability, m}^2 \\
H &= \text{Formation thickness, m} \\
m_0 &= \text{Mass injection rate, kg s}^{-1} \\
\phi &= \text{Porosity} \\
p &= \text{Pressure, Pa} \\
p_i &= \text{Initial pressure, Pa} \\
r &= \text{Radial distance, m} \\
r_0 &= \text{Well radius, m} \\
R &= \text{Formation radius, m} \\
\rho_c &= CO_2 \text{ density, kg m}^{-3} \\
S &= CO_2 \text{ saturation} \\
S_r &= \text{Residual brine saturation} \\
t &= \text{Time, s}
\end{aligned}
\tag{16}
$$

Units are given in the SI system.

A generalisation should consider a non-linear pressure equation, since the permeability depends on the pressure field, meaning that the diffusivity varies with pressure. The reason is that cracks re-open when the pore pressure exceeds a given threshold. There are several permeability-pressure models ranging from exponential laws (e.g., Palmer and Mansoori, 1998) to power laws (Gangi and Carlson, 1996). Shapiro and Dinske (2009) and Hummel and Shapiro (2012) use basically a model similar to that of Gangi and Carlson (1996).

B Fractal failure criterion

We vary the threshold P fractally. Let ΔP_m be the maximum deviation from the background value P_0. P at r is first subjected to the variations $(\Delta P)^r$, such that

$$
-\Delta P_m \leq (\Delta P)^r \leq \Delta P_m,
\tag{17}
$$

where $(\Delta P)^r$ is obtained from a random generator, and the superindex "r" denotes random. (Random numbers between 0 and 1 are generated and then scaled to the interval $[-1, 1]\Delta P_m$.)

The fractal variations can be described by the von Kármán autocovariance function. The exponential function used by Rothert and Shapiro (2003) is a particular case of this function, which is widely used in seismic applications (e.g., Carcione et al., 2003). The corresponding wavenumber-domain spectrum of the von Kármán function.is

$$
S(k_1, k_2) = C(1 + k^2 l^2)^{-(\nu + d/2)},
\tag{18}
$$

where $k = \sqrt{k_1^2 + k_2^2}$ is the wavenumber, l is the correlation length, ν $(0 < \nu < 1)$ is a self-similarity coefficient, C is a normalization constant, and d is the Euclidean dimension. The von Kármán correlation function describes self-affine, fractal processes of fractal dimension $d + 1 - \nu$ at scales smaller than l. **Correlation lengths can be determined from the power spectral density of physical rock properties determined from well-logging data, such as sonic logs (e.g., Holliger, 1997).**

The threshold P is then calculated as

$$P(x, y) = P_0 \pm \Delta P(x, y), \tag{19}$$

where

$$\widetilde{\Delta P}(k_1, k_2) = \widetilde{(\Delta P)}^r (k_1, k_2) S(k_1, k_2,), \tag{20}$$

with $\widetilde{(\Delta P)}^r (k_1, k_2)$ being the Fourier transform of $(\Delta P)^r(x, y)$. (The tilde denotes the space Fourier transform.)

The variation range ΔP around the mean value may determine the number of events. The larger this range the higher this number.

C Viscoelastic differential equations

The time-domain equations for 2D wave propagation in a heterogeneous viscoelastic medium can be found in Carcione et al. (2008) and Carcione (2015). The anelasticity is described by the standard linear solid, also called the Zener model, that gives relaxation and creep functions in agreement with experimental results.

The two-dimensional velocity-stress equations for anelastic propagation in the (x, z)-plane, assigning one relaxation mechanism to dilatational anelastic deformations $(\nu = 1)$ and one relaxation mechanism to shear anelastic deformations $(\nu = 2)$, can be expressed by

i) Euler-Newton's equations:

$$\dot{v}_x = \frac{1}{\rho}(\sigma_{xx,x} + \sigma_{xz,z}) + f_x, \tag{21}$$

$$\dot{v}_z = \frac{1}{\rho}(\sigma_{xz,x} + \sigma_{zz,z}) + f_z, \tag{22}$$

where v_x and v_z are the particle velocities, σ_{xx}, σ_{zz} and σ_{xz} are the stress components, ρ is the density and f_x and f_z are the body forces. A dot above a variable denotes time differentiation.

ii) Constitutive equations:

$$\dot{\sigma}_{xx} = K(v_{x,x} + v_{z,z} + e_1) + \mu(v_{x,x} - v_{z,z} + e_2) + \dot{M}_{xx}, \tag{23}$$

$$\dot{\sigma}_{zz} = K(v_{x,x} + v_{z,z} + e_1) - \mu(v_{x,x} - v_{z,z} + e_2) + \dot{M}_{zz}, \tag{24}$$

$$\dot{\sigma}_{xz} = \mu(v_{x,z} + v_{z,x} + e_3) + \dot{M}_{xz}, \tag{25}$$

where e_1, e_2 and e_3 are memory variables, M_{ij} are moment-tensor components and k and μ are the unrelaxed (high-frequency) bulk and shear moduli, respectively, given by $K = \rho(v_P^2 - 4v_S^2/3)$ and $\mu = \rho v_S^2$, where v_P and v_S are the P- and S-wave velocities.

iii) Memory variable equations:

$$\dot{e}_1 = \left(\frac{1}{\tau_\epsilon^{(1)}} - \frac{1}{\tau_\sigma^{(1)}}\right)(v_{x,x} + v_{z,z}) - \frac{e_1}{\tau_\sigma^{(1)}}, \tag{26}$$

$$\dot{e}_2 = \left(\frac{1}{\tau_\epsilon^{(2)}} - \frac{1}{\tau_\sigma^{(2)}}\right)(v_{x,x} - v_{z,z}) - \frac{e_2}{\tau_\sigma^{(2)}}, \tag{27}$$

$$\dot{e}_3 = \left(\frac{1}{\tau_\epsilon^{(2)}} - \frac{1}{\tau_\sigma^{(2)}}\right)(v_{x,z} + v_{z,x}) - \frac{e_3}{\tau_\sigma^{(2)}}, \tag{28}$$

where $\tau_\sigma^{(\nu)}$ and $\tau_\epsilon^{(\nu)}$ are material relaxation times, corresponding to dilatational ($\nu = 1$) and shear ($\nu = 2$) deformations.

The relaxation times can be expressed as

$$\tau_\epsilon^{(\nu)} = \frac{\tau_0}{Q_\nu}\left(\sqrt{Q_\nu{}^2 + 1} + 1\right), \quad \tau_\sigma^{(\nu)} = \tau_\epsilon^{(\nu)} - \frac{2\tau_0}{Q_\nu}, \tag{29}$$

where τ_0 is a relaxation time such that $1/\tau_0$ is the center frequency of the relaxation peak and Q_ν are the minimum quality factors.

D Tensile and shear sources

The moment-tensor components in 3D space are

$$M_{ij} = M_0 m_{ij}\delta(x)\delta(y)\delta(z)g(t) \tag{30}$$

where M_0 is the moment tensor, δ is Dirac delta and $g(t)$ is the source time history, which satisfies

$$\int_0^\infty |\dot{g}|dt = 1 \tag{31}$$

(Carcione et al., 2014). The discrete version of the moment-tensor components are

$$M_{ij} = \frac{M_0}{dxdydz}m_{ij}g(t), \tag{32}$$

where dx, dy and dz are the grid spacings ($dy =1$ in the 2D case).

The moment-tensor theory describing tensile and shear sources is given, for instance, in Vavryčuk (2011). We have

$$\sqrt{2}\,\mathbf{m} = \begin{pmatrix} 2n_1\nu_1 & n_1\nu_2 + n_2\nu_1 & n_1\nu_3 + n_3\nu_1 \\ n_1\nu_2 + n_2\nu_1 & 2n_2\nu_2 & n_2\nu_3 + n_3\nu_2 \\ n_1\nu_3 + n_3\nu_1 & n_2\nu_3 + n_3\nu_2 & 2n_3\nu_3 \end{pmatrix} \tag{33}$$

where

$$\begin{aligned} n_1 &= -\sin\delta\sin\phi, \\ n_2 &= \sin\delta\cos\phi, \\ n_3 &= -\cos\delta, \end{aligned} \tag{34}$$

$$\begin{aligned} \nu_1 &= (\cos\lambda\cos\phi + \cos\delta\sin\lambda\sin\phi)\cos\varphi - \sin\delta\sin\phi\sin\varphi, \\ \nu_2 &= (\cos\lambda\sin\phi - \cos\delta\sin\lambda\cos\phi)\cos\varphi + \sin\delta\cos\phi\sin\varphi, \\ \nu_3 &= -\sin\lambda\sin\delta\cos\varphi - \cos\delta\sin\varphi, \end{aligned} \tag{35}$$

where here δ, λ and ϕ are the dip, rake and strike angles, respectively, and φ is the slope angle describing the tensility of the source, such that $\varphi = 90^\circ$ for pure extensive sources, $\varphi = 0^\circ$ for shear sources and $\varphi = -90^\circ$ for pure compressive sources. The components satisfy $m_{ij}m_{ij} = 1$, where implicit summation is assumed. This implies the $\sqrt{2}$ normalization in equation (35).

For $\varphi = 0$, we recover the usual moment-tensor components describing shear faulting:

$$\begin{aligned} \sqrt{2}m_{11} &= -(\sin\delta\cos\lambda\sin 2\phi + \sin 2\delta\sin\lambda\sin^2\phi), \\ \sqrt{2}m_{12} &= (\sin\delta\cos\lambda\cos 2\phi + \tfrac{1}{2}\sin 2\delta\sin\lambda\sin 2\phi), \\ \sqrt{2}m_{13} &= -(\cos\delta\cos\lambda\cos\phi + \cos 2\delta\sin\lambda\sin\phi), \\ \sqrt{2}m_{22} &= (\sin\delta\cos\lambda\sin 2\phi - \sin 2\delta\sin\lambda\cos^2\phi), \\ \sqrt{2}m_{23} &= -(\cos\delta\cos\lambda\sin\phi - \cos 2\delta\sin\lambda\cos\phi), \\ \sqrt{2}m_{33} &= \sin 2\delta\sin\lambda. \end{aligned} \tag{36}$$

Here we consider the 2D case and pure tensile and shear sources. In the first case, we assume $\varphi = \lambda = \phi = 90^\circ$, giving

$$\sqrt{2}m_{xx} = 2\sin^2\delta, \quad \sqrt{2}m_{zz} = 2\cos^2\delta, \quad \sqrt{2}m_{xz} = \sin 2\delta, \tag{37}$$

while shear sources are described by $\varphi = 0$ and $\lambda = \phi = 90^\circ$ giving

$$\sqrt{2}m_{xx} = -\sin 2\delta, \quad \sqrt{2}m_{zz} = \sin 2\delta, \quad \sqrt{2}m_{xz} = -\cos 2\delta. \tag{38}$$

E Porous-media model

To obtain the unrelaxed moduli K and μ for partial saturation, we consider Gassmann equations by which

$$K = K_m + \bar{\alpha}^2 M, \tag{39}$$

where $K_m = C_r$, and $\bar{\alpha}$ and M are given in equation (10) (e.g., Carcione, 2015). The effective fluid bulk modulus is given by Wood equation,

$$K_f = \left(\frac{S}{K_c} + \frac{1-S}{K_w} \right)^{-1}, \tag{40}$$

where K_c and $K_w = 1/C_w$ are the bulk moduli of CO_2 and brine, respectively.

On the other hand, the density is

$$\rho = (1-\phi)\rho_s + \phi[S\rho_c + (1-S)\rho_w], \tag{41}$$

where ρ_s, ρ_c and ρ_w are the solid, CO_2 and brine densities, respectively.

Then, the P- and S-wave velocities are given by

$$v_P = \sqrt{\frac{K + 4\mu_m/3}{\rho}} \quad \text{and} \quad v_S = \sqrt{\frac{\mu_m}{\rho}}, \tag{42}$$

respectively.

A more refined and accurate method is to consider the poro-viscoelastic model used in Carcione et al. (2012) and based on White mesoscopic theory, which also gives a physical estimations of the loss parameters Q_1 and Q_2.

F Location of sources. Reverse-time migration

Sources can be located by a reverse-time migration algorithm for instance (McMechan, 1982), although the wave equation given in appendix C cannot be back propagated with ease due to the presence of seismic attenuation. First, it is difficult to obtain an attenuation model from seismic data with enough accuracy to correct for amplitude loss and velocity dispersion. Second, that equation is not time reversible, although there are a few techniques based on Q compensation to deal with seismic loss in migration algorithms, e.g., Zhu et al. (2014).

A time-reversible 2D elastic wave equation is the impedance-matching equation

$$\ddot{v}_x = c_P \partial_x c_P \left(\partial_x v_x + \partial_z v_z \right) - 2c_S \partial_x c_S \partial_z v_z + c_S \partial_z c_S \left(\partial_z v_x + \partial_x v_z \right),$$
$$\ddot{v}_z = c_P \partial_z c_P \left(\partial_x v_x + \partial_z v_z \right) - 2c_S \partial_z c_S \partial_x v_x + c_S \partial_x c_S \left(\partial_z v_x + \partial_x v_z \right) \tag{43}$$

(Carcione et al., 1994), where ∂_i is the spatial derivative with respect to x_i and c_P and c_S are the P- and S-wave velocities. Since each discontinuity at the subsurface can generate unwanted secondary fields, it is desirable to suppress these effects. Equation (43) is the result of using the density as a parameter so that there is no discontinuity in acoustic impedance.

If the wave field can be separated into P and S waves (e.g., Robertsson and Curtis, 2002), so that these fields can be migrated separately, the wave equation for each mode is

$$\ddot{\psi} = c \left(\partial_x c \partial_x + \partial_z c \partial_z \right) \psi, \tag{44}$$

(Carcione et al., 2003; Gajewski and Tessmer, 2005), where c is the wave velocity, which may correspond to P waves or to S waves.

The discretization of equation (44) in a uniform mesh with square cells and based on a $O(2, \infty)$-scheme is

$$\frac{\psi_{i,j}^{n+1} - 2\psi_{i,j}^{n} + \psi_{i,j}^{n-1}}{dt^2} = c \left(\partial_x c \partial_x + \partial_z c \partial_z \right) \psi \tag{45}$$

(e.g., Abramowitz and Stegun, 1964), where $t = ndt$ and the spatial derivatives are computed with the Fourier pseudospectral method, as in Baysal et al. (1983).

Back-propagation is performed from (45) as

$$\psi_{i,j}^{n-1} = 2\psi_{i,j}^n - \psi_{i,j}^{n+1} + cdt^2 \left(\partial_x c \partial_x + \partial_z c \partial_z \right) \psi. \tag{46}$$

The elastic wave equation (43) can easily be discretized and its back-propagation version obtained in the same manner. In the migration process, the seismogram is a time-dependent boundary condition in equation (46). The time step dt is equal to the sample rate of the data. The seismic trace is applied at each receiver in reverse time and the propagation goes back in time until the origin time, where the best focusing occurs. The reverse modeling sums the energy of all receivers, enhancing the signal-to-noise ratio.

The imaging condition is that of Gajewski and Tessmer (2005), i.e., the origin times of the events are given by the time where maximum focusing (maximum amplitude) occurs. In our case, this is performed for each grid point of the mesh and we choose a number of sources whose relative amplitudes exceed a given threshold. The problem is that the sources are not synchronous. A simple method applied here considers the maximum amplitudes at the grid as a function of the back propagation time.
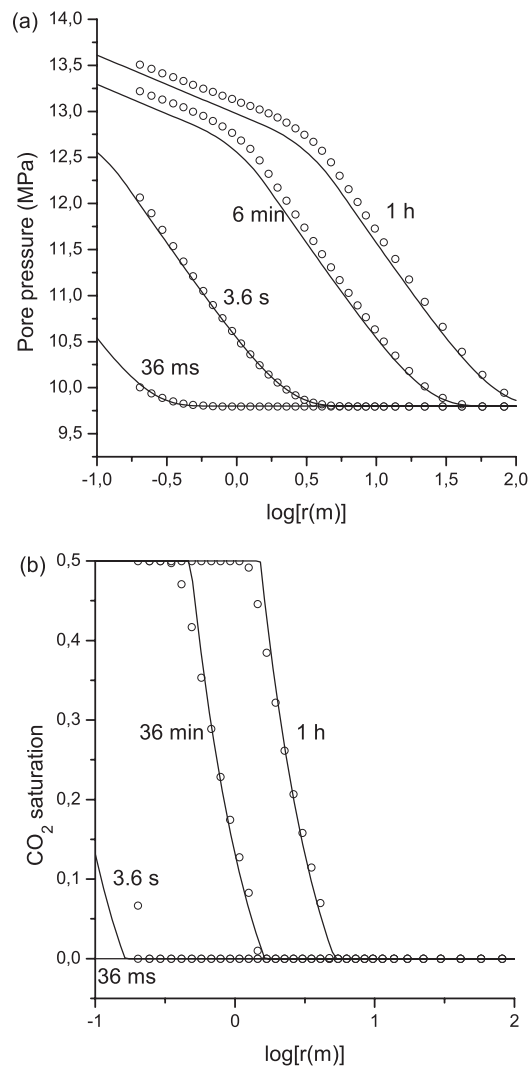
Fig. 1 CO$_2$ injection in sand. Pressure (a) and saturation (b) profiles as a function of the radial distance from the well at different injection times, where the solid lines correspond to the analytical solution and the open circles refer to simulations obtained with the commercial software TOUGH2 ECO2N. The fluids are immiscible.
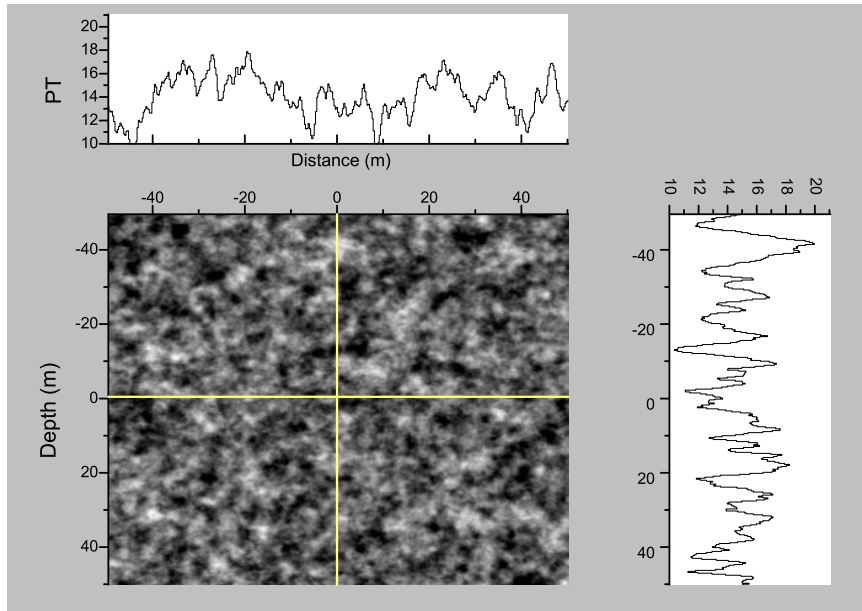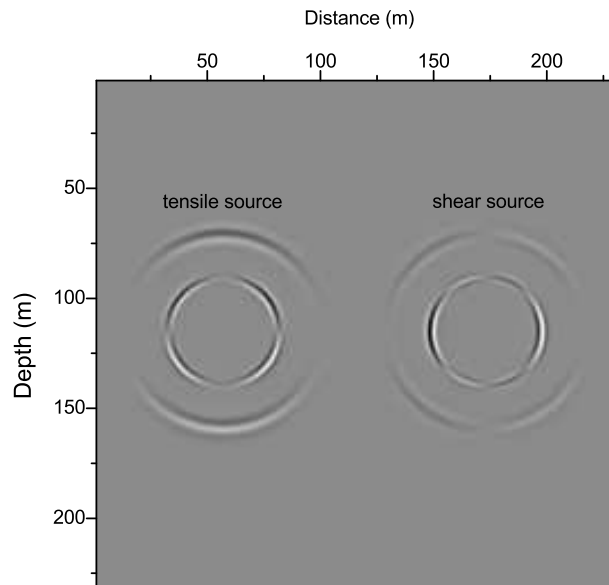
**Fig. 2** Random distribution of the failure criterion P_T (in MPa) based on the Young modulus. The medium is divided into 375×375 cells.

20
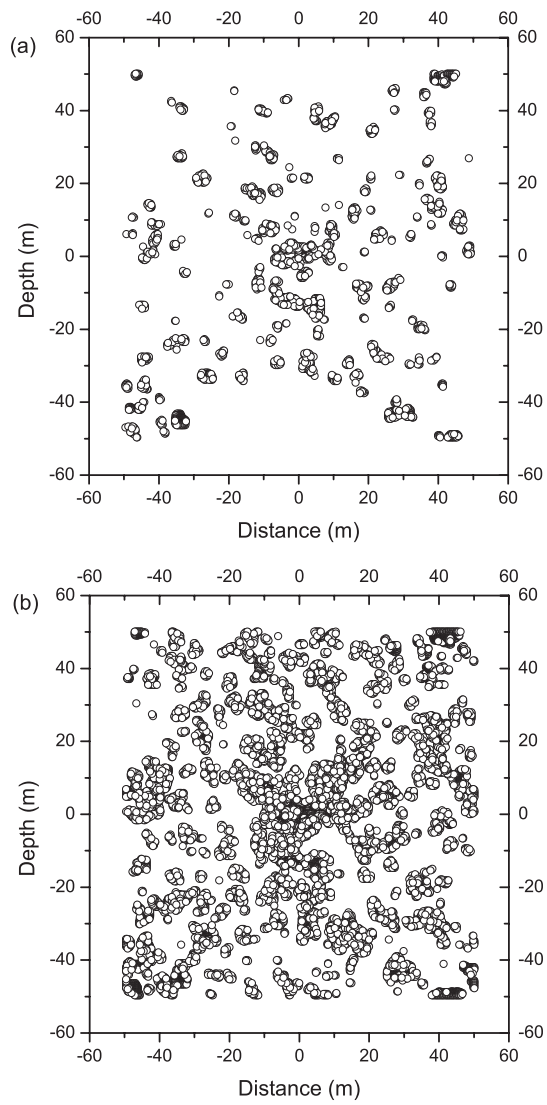
Fig. 3 Cloud of tensile (a) and shear (b) events
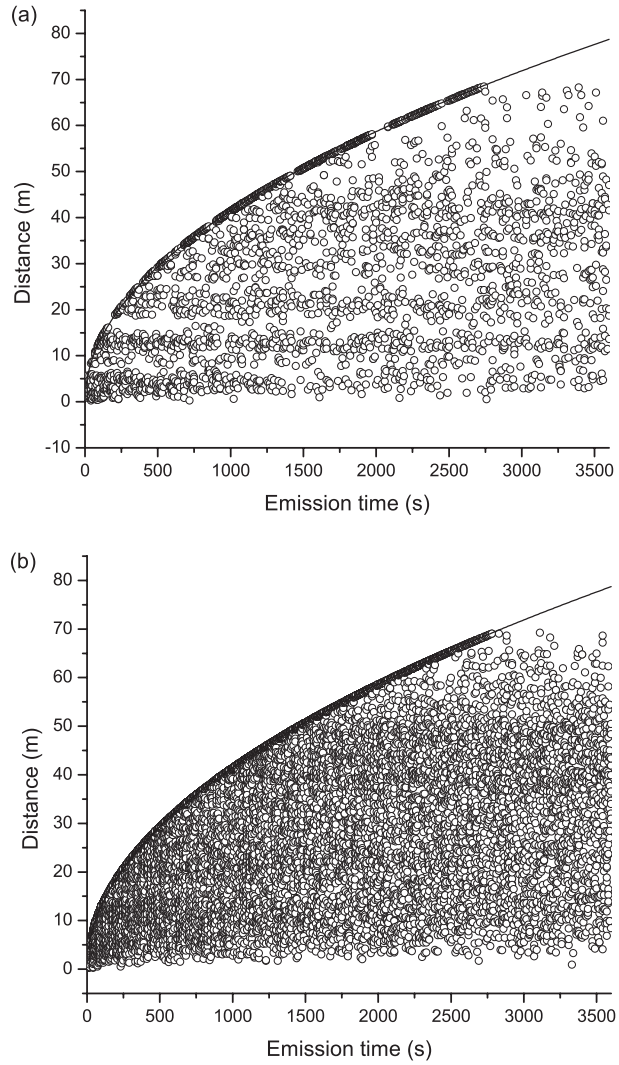
Fig. 4 Location of the tensile (a) and shear (b) events as a function of the emission time, where the solid lines corresponds to equation (8) with $D = 0.137$ m^2/s.

Fig. 5 Snapshot of the vertical component of the particle velocity at 0.4 s, showing the radiation patterns of the tensile and shear sources. The maximum value is 8.4 mm/s
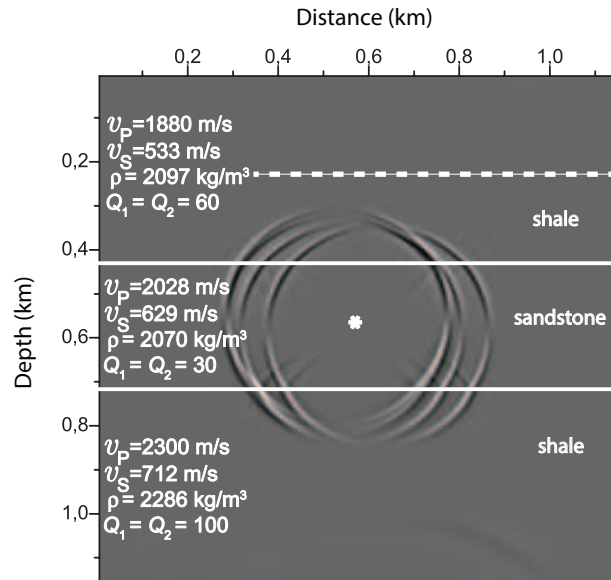
Fig. 6 Geological model and snapshot at 3000.05 s, where three shear sources and one tensile source are active. The unrelaxed velocities, density and loss parameters are shown. The star indicates the injection point and the dashed line represents the receivers.

(a)

(b)
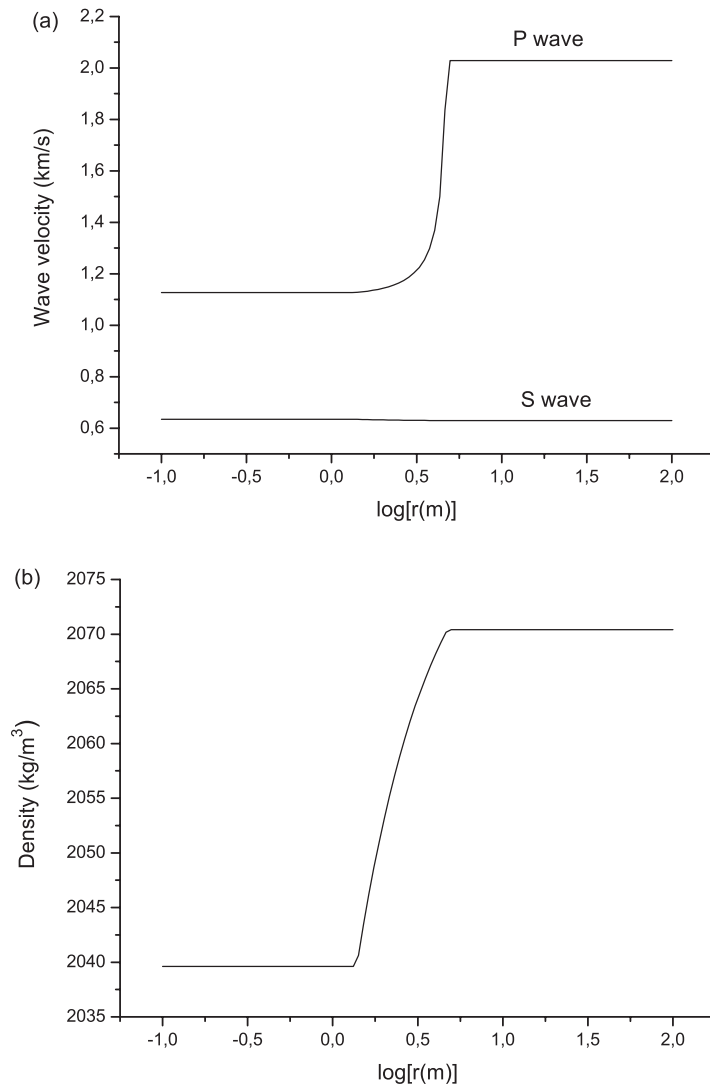
Fig. 7 Unrelaxed wave velocities and density as a function of the radial distance at 3000 s from the onset of injection.
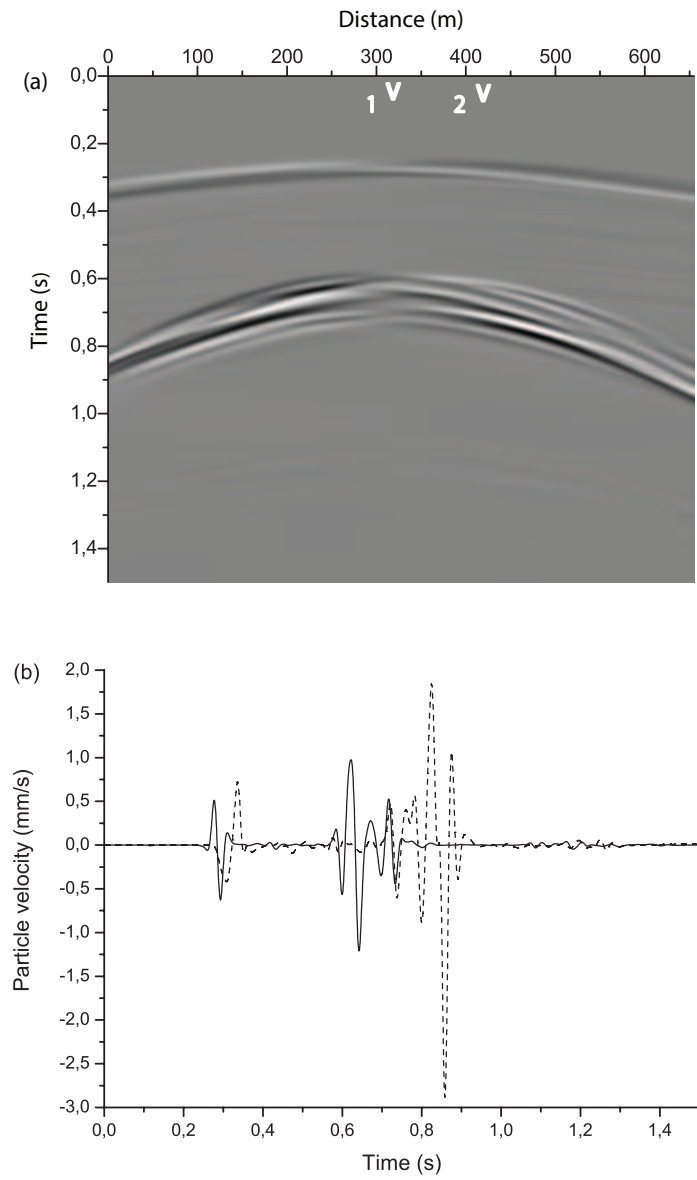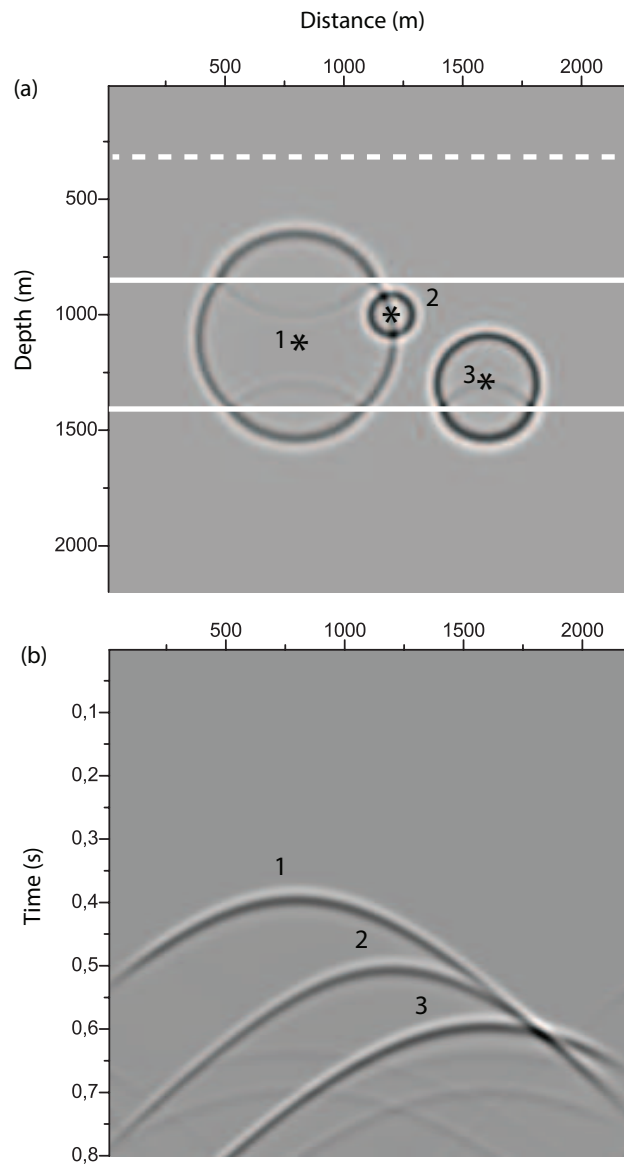
Fig. 8 Synthetic seismogram (a) and time history at the two receivers indicated with a V letter (b); receiver 1 (solid line) and receiver 2 (dashed line).
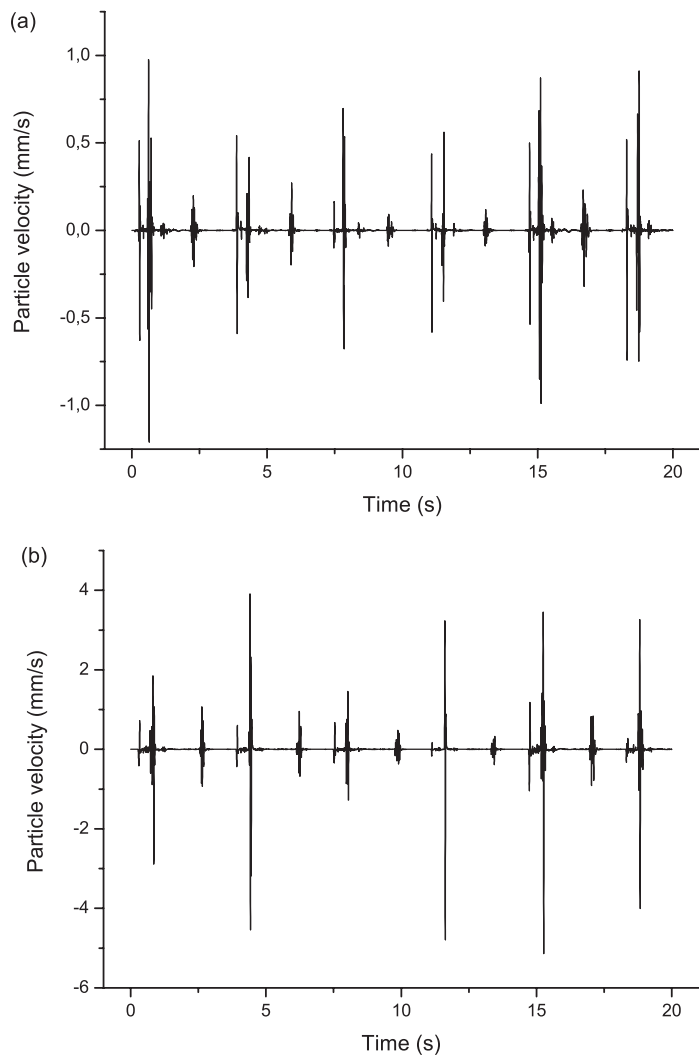
Fig. 9 Time histories recorded at receivers 1 (a) and 2 (b) shown in Figure 8. The media are lossless.
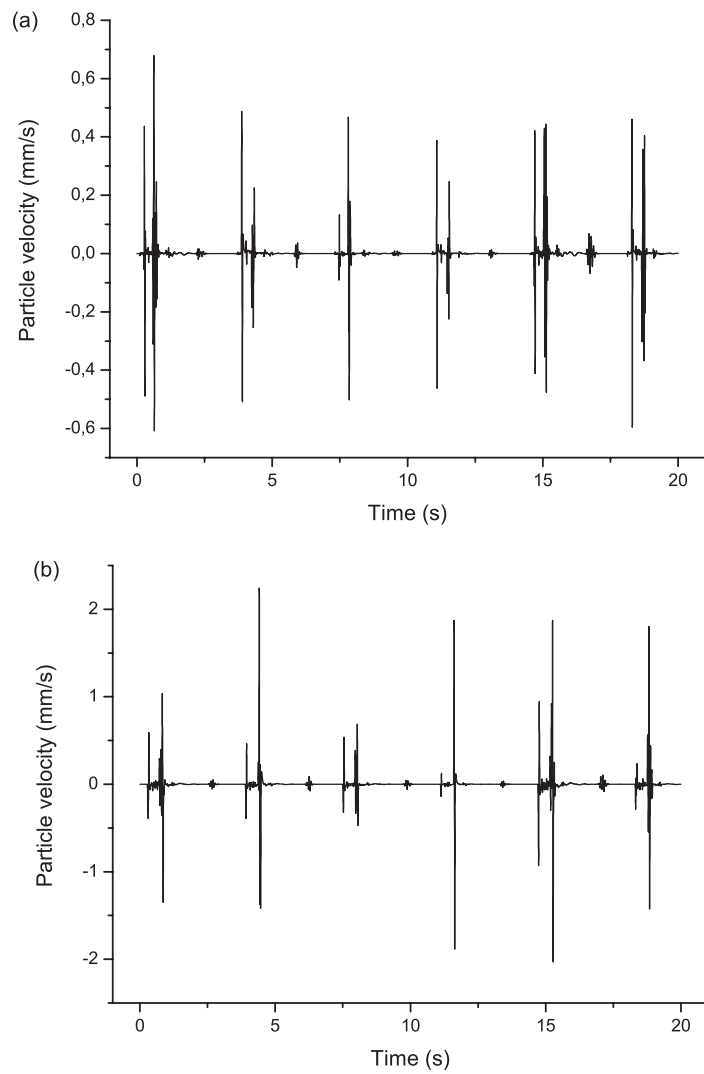
Fig. 10 Time histories recorded at receivers 1 (a) and 2 (b) shown in Figure 8. The media are lossy.

Fig. 11 Snapshot (a) and seismogram (b) corresponding to three sources activated at different onsets. The location of the sources are indicated by stars and the seismic events are labeled by the source that has generated them. The dashed line are the receivers.
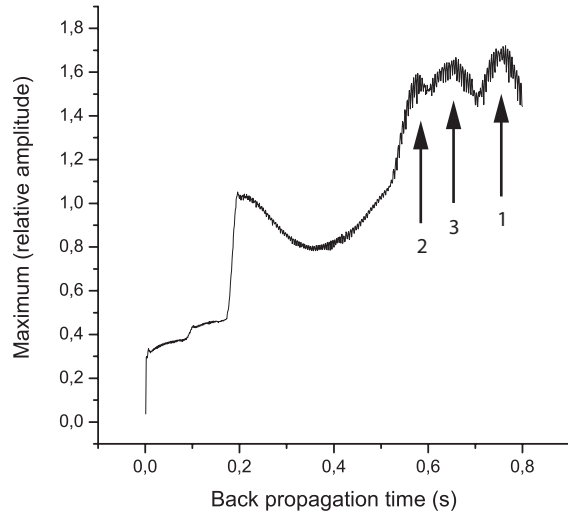
Fig. 12 Wave field maxima at the images obtained by reverse-time migration as a function of the back propagation time. The numbers correspond to the the sources in Figure 11.
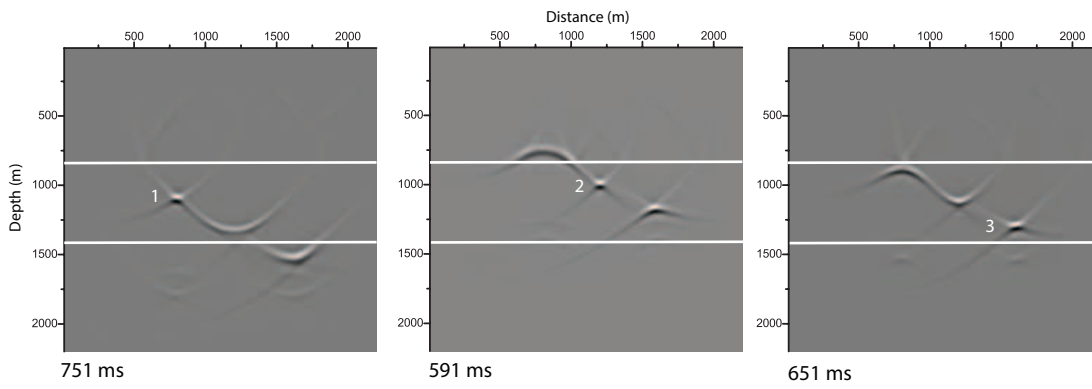
Fig. 13 Reverse-time migration images at different back propagation times, where the wave field has been focused at each source location. The numbers indicate the sources.